Indian Journal of Pure & Applied Physics
Vol. 59, July 2021, pp. 496-503

Micro-Structure and Vibrational Mode of Complex Double Perovskite Oxides $xLaAlO_3 – (1\text{-}x)Ba(Mg_{1/2}W_{1/2})O_3$

B Patra[a], B Ghosh[*b], S Banerjee [a] & T P Sinha[c]

[a]Department of Physics, University of Calcutta, 92 Acharya Prafulla Chandra Road, Kolkata -700 009, India

[b]St. Paul's Cathedral Mission College, 33/1 Raja Rammohan Roy Sarani, Kolkata -700 009, India

[c]Department of Physics, Bose Institute, 93/1 Acharya Prafulla Chandra Road, Kolkata -700 009, India

Received 4 November 2020; accepted 9 April 2021

The micro-structures and vibrational modes of complex double perovskite oxides $xLaAlO_3 – (1\text{-}x)Ba(Mg_{1/2}W_{1/2})O_3$[LA-BMW] have been characterized for different values of x (0.10, 0.25, 0.50, 0.75 and 0.90). The materials are synthesized by the solid state reaction technique. The Rietveld refinement of the XRD patterns shows rhombohedral $R\bar{3}C$(161) phase for $LaAlO_3$ and cubic Fm3m (225) phases for $Ba(Mg_{1/2}W_{1/2})O_3$. XRD patterns show that with increasing the doping concentration 'x', rhombohedral phase gradually increases and cubic phase gradually decreases. A meticulous comparison of crystal structures and vibrational degrees of freedom in the light of change in doping concentration 'x' for LA-BMW has been carried out for accurate identification of crystal symmetry and distortions. From room-temperature comparative Raman spectra of the samples, different vibrational phonon modes have been assigned using group theoretical analysis together with experimental literature survey.

Keywords: Complex double perovskite oxides, Crystal structure, Phonon modes

1 Introduction

The transition metal based rare earth perovskite oxides ABO_3 (where A is the rare earth and B is the transition metal cation) have been extensively studied for varied advanced technological applications such as solid oxide fuel cells, catalyst, chemical detector and sensor, magnetic and conductor material, electrode material, *etc*[1-5]. In double perovskite oxide $A_2B'B''O_6$ material electronic properties depends on cation ordering and interplay as well as interaction between the two types of cations. Order disorder phenomena influence the electrical properties of the materials[6,7] to a great extent. In case of simple perovskite material having chemical formula ABO_3 the electrical conductivity is also governed by B-O-B chains[8-11], and for $A_2B'B''O_6$ the dependence is on B'-O-B" chains[12-19]. With the wealthiness of functional useful properties, complex transition metal oxides are a rich research ground for physicists, engineers, and materials scientists. Additionally, even more exciting is the possibility of combining the properties of individual oxides into varied heterostructures, thereby making artificial multifunctional materials. It is already reported from an earlier study that the complex double perovskite $BaTiO_3–Ba(Mg_{1/2}W_{1/2})O_3$ has a very low dielectric loss[20]. The dielectric properties of these materials are sensitive to slight difference and changes in the composition, crystallographic structure and microstructure of the material. Lanthanum aluminate ($LaAlO_3$; LA) is reported to be a promising candidate as the substrate for the high temperature superconductor (HTS) filter[21]. It is required and desirable to decrease the dielectric loss of the LA in order to improve the properties of the HTS filter.

Moreover, structural and electronic properties of cubic Ba_2MgWO_6 doped with elements like Mo, Ti, La, Nd, Eu, Er, and Lu have already been investigated within the scope of density functional theory. The doping with rare-earth ions leads to a metallic character and the complex structure of the 4f contributes to the density of states of the resulting materials. Such systems with an oxygen vacancy included exhibit a reduced oxidation state of dopant ions and formation of extra bands below the conduction band minimum of the host Ba_2MgWO_6 material[22]. Double perovskite Ba_2MgWO_6 has conjointly been used as a unique host material sensitised with phosphors and Eu^{3+} luminescence properties[23].

*Corresponding author (E-mail: ghosh.binita@gmail.com)

Keeping in mind the utility of Ba_2MgWO_6 as a host material we have synthesised the same and have chosen $LaAlO_3$ as dopant to prepare the complex double perovskite oxides $xLaAlO_3$–$(1-x)Ba(Mg_{1/2}W_{1/2})O_3$ *i.e*. LA-BMW taking various compositions having x values 0.10, 0.25, 0.50, 0.75 and 0.90. We intend to study the dielectric, optical and first principles study of this complex double perovskite. For this we first need to know the exact structure with all the refinement parameters of the series material. Also it is important for us to know how the structure changes with increase in doping concentration.

In this paper we have presented a comparative study of the crystal structures and vibrational degrees of freedom with change in doping concentration 'x' for LA-BMW for accurate identification of crystal symmetry and distortions. Earlier studies show that LA exhibits the rhombohedral symmetry with space group $R\bar{3}C(161)$[24], and BMW crystallizes in cubic symmetry with phase group $Fm3m(225)$[20].

2 Experimental Details

2.1. Sample preparation

The materials were synthesized by the conventional solid state reaction technique by mixing individual high purity (99.9%) powders of La_2O_3 (Aristo), Al_2O_3 (SRL), $BaCO_3$ (LOBA chemie), MgO (LOBA chemie) and WO_3 (LOBA chemie). The starting materials were mixed stoichiometrically in the acetone medium for 12 hr using agate mortar and pestle. The mixtures were calcined in an alumina crucible at 1523K for 10 hr in air and bought to room temperature by cooling at the rate of 3.39 K/min. The calcined samples were pelletized into a disc (diameter ~ 7.6 mm) using 2% polyvinyl alcohol as binder. Finally, the discs were sintered at 1573K for 10 hr and cooled down to room temperature by cooling at the rate of 2.15 K/min.

2.2. Sample characterization

The room temperature X-ray diffraction (XRD) patterns of the materials were taken over a range of Bragg's Angles $(10^\circ - 80^\circ)$, using Cu-K_α radiation by Rigaku Miniflex-II automatic X-ray powder diffractometer. The determinations of lattice parameters and the identifications of the phase of the samples were carried out by the refinement of the XRD pattern using the Rietveld method with the Fullprof program. Scanning electron micrograph (SEM) images were collected by using Carl Zeiss, EVO-18 (Special edition) scanning electron microscope. The pellets were broken and mounted on aluminium stubs. A silver conductive glue was applied such that the samples were grounded to the stub to reduce the electron charging of the samples inside the SEM chamber. The samples were then finely coated with gold to make them conducting to the incident beam of electrons inside the chamber. The prepared samples were then placed in vacuum inside the SEM chamber and an incident electron beam of 20 kV was used to illuminate the samples. The SEM micrographs for the samples were obtained at magnifications of 30000. Dynamic light scattering (DLS) data of the materials were taken by using ZEN1600 at room temperature for measuring the grain size. The room-temperature comparative Raman spectra of these material were studied at an excitation wavelength of 488 nm. In the spectra, peaks for LA *i.e*. for rhombohedral $R\bar{3}C$ phase were observed and for BMW *i.e.* cubic $Fm3m$ phase group were observed.

3 Results and Discussions

3.1 Structural and microstructural characterization

The room temperature XRD patterns of LA-BMW samples are shown systematically in Fig. 1. The Rietveld refinement of the XRD patterns as shown by the solid (black) lines was done with the help of Fullprof program. The background data was fitted with a 6-coefficients polynomial function, and pseudo-Voigt profiles were chosen for the peak shapes. Throughout the refinement, scale factor, lattice parameters, positional coordinators (x, y, z) and the thermal parameters were varied. It is clear from our refinement data that all the samples exist in two phases simultaneously. Both rhombohedral $R\bar{3}C(161)$ and cubic $Fm3m$ (225) phases are found to present in LA-BMW material. A pure rhombohedral phase of $R\bar{3}C$ (161) crystal symmetry of the perovskite structure was obtained in the entire compositional range of LA. Our observation is similar to previously reported structure for LA[24]. The phase structure of the BMW ceramics exhibited a cubic perovskite structure of $Fm3m$ (225) space group. BMW is the main crystalline phase, which is accompanied by small amounts of $BaWO_4$ and Ba_2WO_5 as secondary phases. The impurity peaks of $BaWO_4$ and Ba_2WO_5 are found at 26.3°, 43° and 28° respectively. Here also our observation is similar to previously reported crystal structure for BMW[25, 26]. The X-ray diffraction patterns of the BMW ceramics

did not significantly vary with sintering temperature. The peak at 31.1˚ in Fig. 1 is due to BMW and the peak at 33.4˚ is due to LA. At 50-50 composition both the peaks have comparable intensity. The lattice parameters, bond angles, bond lengths and the goodness of fitting parameters are given in Table 1a and 1b. Bond angle of rhombohedral phase *i.e.* for LA $\alpha = \beta = 90^{\circ}$, $\gamma = 120^{\circ}$ and for cubic phase *i.e* for BMW $\alpha = \beta = \gamma = 90^{\circ}$. It is clearly seen from the Fig. 1 that with increasing the value of x rhombohedral phase gradually increases and cubic phase gradually decreases. Fig. 2 shows a schematic representation of the unit cell of (a) LA, (b) BMW and (c) LA-BMW.

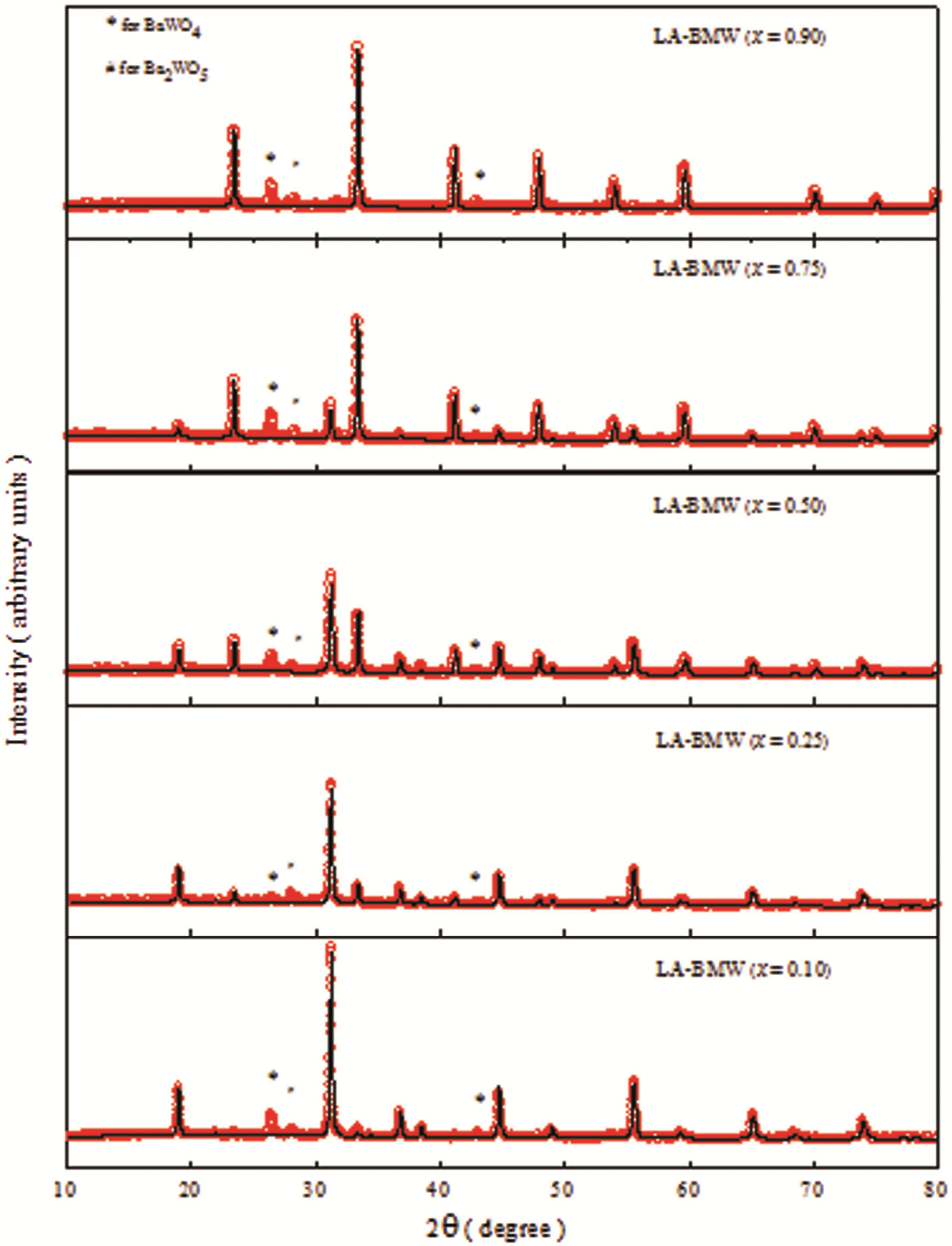

Fig. 1 — Rietveld refinement plot of LA-BMW at room temperature.

The relative integrated intensities of LA, BMW, $BaWO_4$ and Ba_2WO_5 were calculated from the most intensive lines of each phase in the XRD pattern with the help of the following relation,

$$\text{Relative intensity of LA} = \frac{I_{LA}}{I_{LA} + I_{BMW} + I_{BaWO_4} + I_{Ba_2WO_5}} \quad \ldots (1)$$

Other phases were also calculated in the similar way and the results are shown in Table 2.

Table 1(a) — X-ray Diffraction Fitting and Structural Parameters of LA-BMW.

Sample Name	Phase(%)	a(Å)	b(Å)	c(Å)	χ^2
LA-BMW	Rhombohedral(6.99)	5.2109	5.2109	13.3374	3.58
(*x*=0.10)	Cubic(93.01)	8.1003	8.1003	8.1003	
LA-BMW	Rhombohedral(25.08)	5.3734	5.3734	13.1222	1.96
(*x*=0.25)	Cubic(74.92)	8.0999	8.0999	8.0999	
LA-BMW	Rhombohedral(50.24)	5.3592	5.3592	13.1529	2.51
(*x*=0.50)	Cubic(49.76)	8.0995	8.0995	8.0995	
LA-BMW	Rhombohedral(85.44)	5.3719	5.3719	13.1450	3.46
(x=0.75)	Cubic(14.56)	8.1078	8.1078	8.1078	
LA-BMW	Rhombohedral(99.73)	5.3701	5.3701	13.1323	2.84
(*x*=0.90)	Cubic(0.27)	8.4009	8.4009	8.4009	

Table 1(b) — Bond angles and Bond lengths of LA-BMW.

Sample Name	Bond Angle		Bond Length				
	Ba-O-Mg	Ba-O-W	La-O	Al-O	Ba-O	Mg-O	W-O
LA-BMW(x=0.10)	90.2	89.8	2.830	2.100	2.864	2.017	2.033
LA-BMW(x=0.25)	91.67	91.67	2.680	1.897	2.865	1.941	1.941
LA-BMW(x=0.50)	89.96	90.04	2.680	1.900	2.864	2.026	2.023
LA-BMW(x=0.75)	86.6	93.00	2.685	1.899	2.872	2.197	1.860
LA-BMW(x=0.90)	86.53	93.47	2.684	1.901	2.976	2.281	1.920

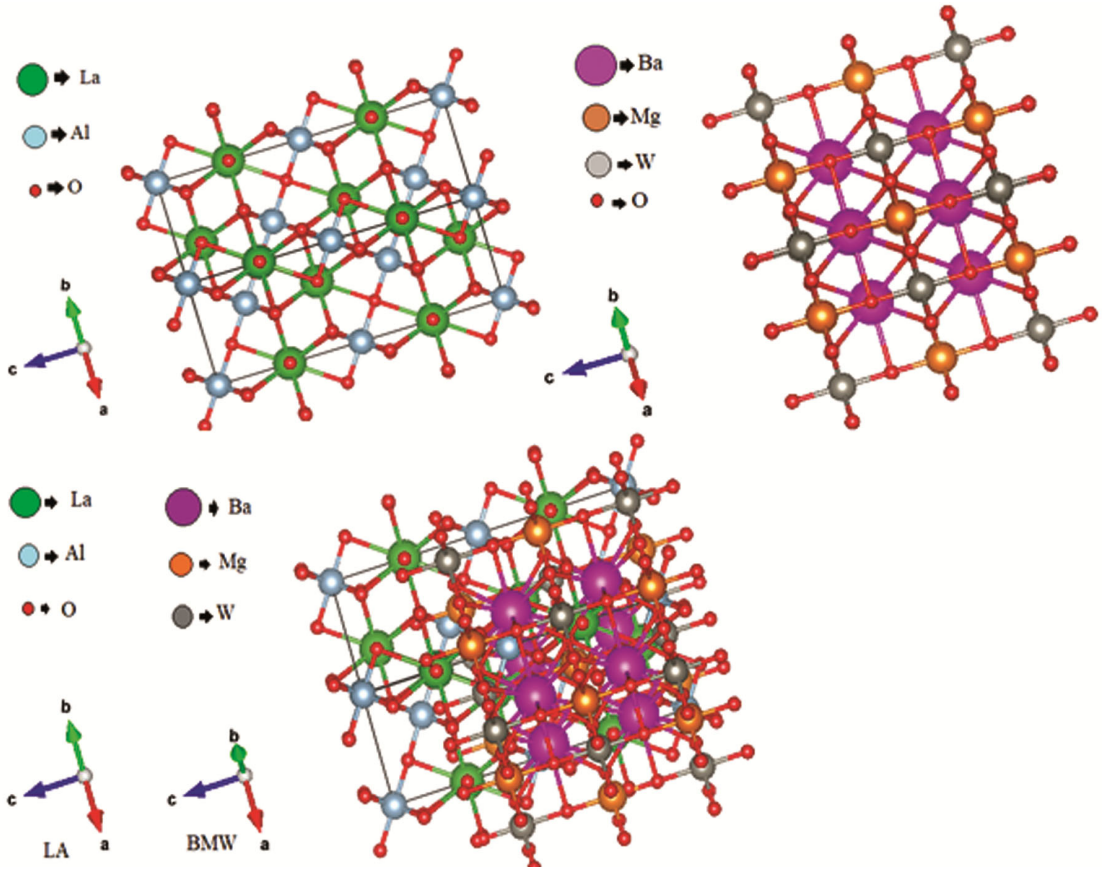

Fig. 2 — A schematic representation of the unit cell.

Table 2 — Relative percentage intensity LA(%), BMW(%), $BaWO_4$(%), and Ba_2WO_5(%) of LA-BMW.

Material	LA (%)	BMW (%)	$BaWO_4$ (%)	Ba_2WO_5 (%)
LA-BMW (x=0.10)	5.9	77.6	11.5	4.9
LA-BMW (x=0.25)	13.4	70.1	7.2	9.2
LA-BMW (x=0.50)	31.3	51.9	11.3	5.5
LA-BMW (x=0.75)	59.1	19.5	14.9	6.4
LA-BMW (x=0.90)	76.9	4.8	12.9	5.4

3.2. SEM and DLS

The typical SEM image of LA-BMW for x = 0.75 is shown in Fig. 3(a). Other images for x = 0.10, 0.25, 0.50, and 0.90 were also taken and their grain sizes were measured. As shown in the SEM image the grains are clearly observed.

For Dynamic light scattering (DLS)[27] data of the materials, small amount of the samples were taken in millipore water and sonicate the mixture for 30 minutes. Then the mixture was taken in a cuvette and the data were taken by using ZEN1600, Si.No. MAL1022382 at room temperature for measuring the grain size. DLS data of LA-BMW for different values of x are plotted in Fig. 3(b). From this plot we get an idea of the grain size distribution. Comparison of grain size that are obtained from SEM and DLS are shown in the Table 3. From the analysis of the SEM data along with DLS, it is found that the sample size range in between 300 to 1500 nm.

3.3 Raman spectroscopy

The room-temperature comparative Raman spectra of LA-BMW for x = 0.10, 0.25, 0.50, 0.75 and 0.90 are displayed in Fig. 4. In this material LA shows rhombohedral $R\bar{3}C$ phase and BMW shows cubic Fm3m phase group and another two phase stetragonal and cubic appear for $BaWO_4$[25] and Ba_2WO_5[28]. It is clear from the crystal structure that Mg and W atoms are centered at different octahedral sites and provide only infrared active modes (F_{1u}). Raman active modes come from Ba and O atoms at 8c and 24e Wyckoff sites, following the representation A_{1g}, E_g, and F_{2g}. From this distribution, four Raman and four infrared active modes are expected to appear in the vibrational spectra of BMW compound.

In the rhombohedral LA of space group $R\bar{3}C$, the La atoms occupy the (0,0, $^1/_4$) and (0,0,0) positions

Table 3 — Comparison between grain size of LA-BMW from SEM and DLS.

Sample Name	DLS (n.m.)	SEM (n.m.)
LA-BMW (x=0.10)	1106	1228
LA-BMW (x=0.25)	533	310
LA-BMW (x=0.50)	770	533
LA-BMW (x=0.75)	1279	1042
LA-BMW (x=0.90)	1483	1062

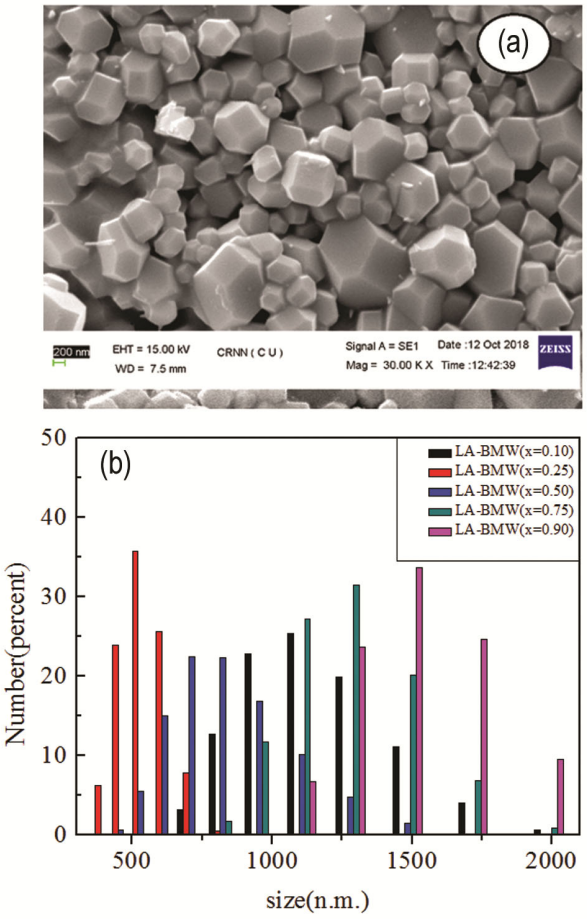

Fig. 3 — (a) SEM images of LA-BMW for x=0.75. (b) DLS plot of LA-BMW.

which participate in phonon modes $(A_{2g} + A_{2u} + E_g + E_u)$ and $(A_{1u} + A_{2u} + 2E_u)$. The oxygen atoms occupy the positions $(^1/_2, o, ^1/_4)$ and take part in twelve modes $(A_{1g} + A_{1u} + 2A_{2g} + 2A_{2u} + 3E_g + 3E_u)$. Here, subscripts g and u represent symmetric and antisymmetric modes with respect to centre of inversion. Among all the total 20 G-point modes, there are 18 optical phonon modes. The $A_{1g} + 4E_g$ modes are only Raman active and the $3A_{2u} + 5E_u$ are only infrared active, and the remaining $2A_{1u} + 3A_{2g}$ modes are inactive modes.

In the BMW cubic phase group Fm3m Ba atoms occupy the $(1/4, 1/4, 1/4)$ positions, Mg atoms occupy the $(0,0,1/2)$ positions, W atoms occupy the $(0,0,0)$ positions and O atoms occupy the $(1/4, 0, 0)$ positions. Standard group theory analysis shows that for the Fm3m space group, the following zone-centre lattice modes and optical activities are present[29, 30].

$$\Gamma_i = A_{1g}(R) + E_g(R) + 2T_{2g}(R) + T_{1g}(S) + T_{2u}(S) + 4T_{1u}(IR) + T_{1u}(ac) \quad \ldots (2)$$

In addition to one three-degenerate acoustic (ac) mode, there are four Raman-active (R), four infrared-active (IR) and two optically inactive or silent (S) modes. Raman-active A_{1g} and E_g modes correspond to a displacement of the oxygen atoms along the linear W-O-Mg axis[31]. Here, Ba atoms at the A site are not allowed to move, since their phonon contribution at Γ-point is $F_{1u} \oplus F_{2g}$. It is to be noted that such a mode also depends on the W–O bond strength. So their frequencies are primarily determined by the Mg-O and W-O interatomic distances and bonding energies, and the chemical nature of W and Mg octahedral cations Four IR-active modes belong to the representation T_{1u} and all atoms are allowed to move during these vibrations. In the 1:1 ordered cubic perovskites, the $\mathbf{A}_{1g}$ breathing mode induces a one-phonon behavior, unlike the case of the 1:2 ordered system where the two-phonon behaviour for A_{1g} exists. The disorder usually appears as anti-site defects in which 4a and 4b positions are partially filled by B′ and B″ cations. It means that the effect of disorder can be seen by following the peak parameters such as intensity, position and peak width. Therefore, partially disordered perovskites only exhibit breathing modes with broadening due to the damping and a downshift attributed to the anti-site defects that introduce a variation in the (B′,B″)–O force constant value. If we closely look at our Fig. 4(a), we see that the A_{1g} peak at around 146 cm^{-1} gradually broadens as the doping concentration increases. This means that the ordering is disturbed with increase in concentration.

From the group theoretical analysis the different phonon modes for $BaWO_4$ is as follows[16].

$$\Gamma = 3A_g + 5B_g + 5E_g + 5A_u + 3B_u + 5E_u \quad \ldots (3)$$

The Raman active modes are $3A_g + 5B_g + 5E_g$, and therefore, 13 first-order Raman lines should be observed[32]. Table 4, 5, 6 and 7 give a detailed report of the different phonon modes of the samples.

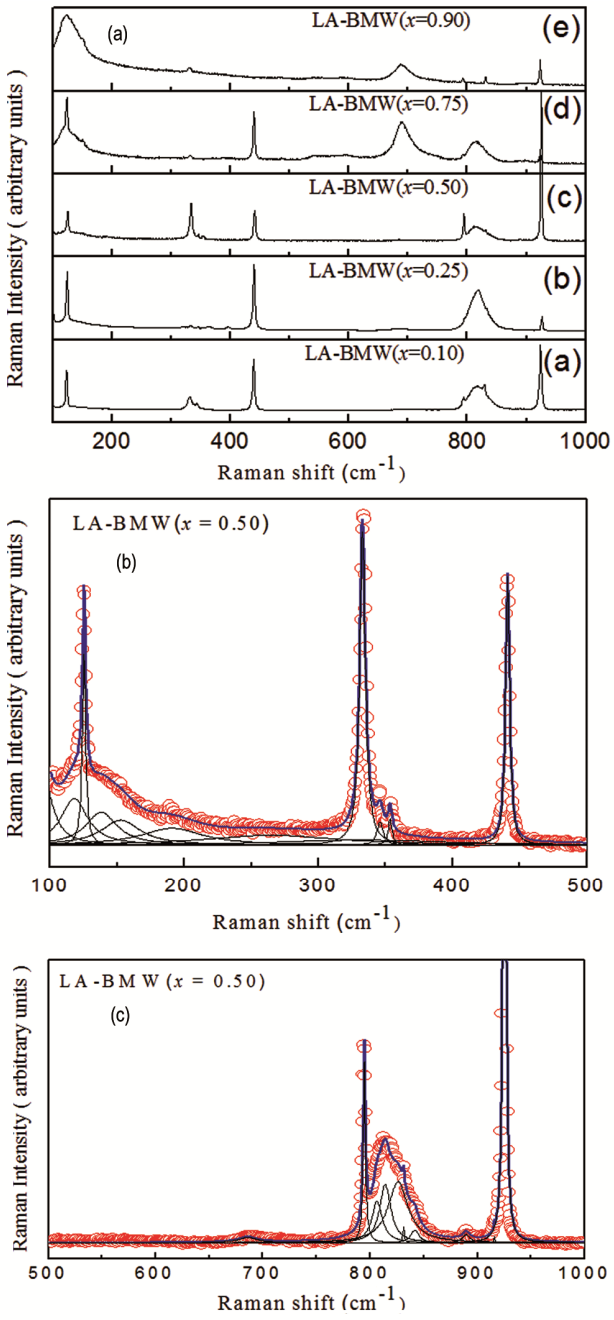

Fig. 4 — Room temperature Raman spectra of (A) LA-BMW(x=0.10, 0.25, 0.50, 0.75 and 0.90). (B) and (C) are the Typical Fitting for x=0.50, where open red circles represent experimental data and solid blue line represent deconvoluated phonon mode adjusted by Lorentzian curves.

Table 4 — Phonon frequencies of LA

Mode	Observed values(cm^{-1})
A_{1g}	146(e)
E_g	185(a), 191(c), 195(e)
E_g	497 cm^{-1} (e)
E_g	694(a), 684 cm^{-1}(b), 689 cm^{-1}(d), 689 cm^{-1}(e)
E_g	486 cm^{-1} (e)

Table 5 — Phonon frequencies in cm^{-1} of BMW with compared to the experimental data from reference[28].

EXPT.	IR-active modes(cm^{-1})				Raman-active modes(cm^{-1})		Silent modes(cm^{-1})	
	T_{1u}(I)	T_{1u}(II)	T_{1u}(III)	T_{1u}(IV)	T_{2g}(I)	T_{2g}(II)	A_{1g}	T_{2u}
	149(a)	295(a)	365(b)	594(d) 591(e)	124(a)	440(a)440(b)	808(a)	184(a)
	153(c)	258(b)	366(e)		125(b)	441(c)	804(b)	179(b)
	151(d)	265(c)			125(c)	440(d)	806(c)	
		290(e)			124(d)			
					122(e)			
Ref. [28]	149	321	381	618	126	441	813	

Table 6 — Comparison between reported values of several Raman active phonon frequencies (cm^{-1}) and observed ones of $BaWO_4$.

Mode	Reported values[27]	Observed values
$T(B_g)$	140.60	135(a), 138(c), 134(d)
$T(A_g)$	145.10	143(b)
$T(E_g)$	219.20	223(d)
$\nu_2(A_g)$	327.43	343(a), 333(b), 346(c),
ν_2 (B_g)	327.40	332(a),320(b), 333(c), 332(d), 332(e)
$\nu_4(B_g)$	332.00	353(a), 345(b), 354(c)
$\nu_4(E_g)$	383.90	391(d)
$\nu_3(E_g)$	814.00	819(a), 819(b), 815(c), 814(d)
$\nu_3(B_g)$	844.00	839(a), 838(b), 842(c), 836(d), 831(e)
$\nu_1(A_g)$	921.00	924(a), 927(b), 925(c), 923(d), 923(e)

Table 7 — Phonon frequencies in cm^{-1} of Ba_2WO_5 with compared to the experimental data from reference[27].

Mode	Reported values	Observed values
	883, 904	887(a), 891(b) 889(c), 898(d), 897(e)
$\nu_1(A_g)$	848, 838	830(a), 831(c), 825(d)
ν_2	758,754	794(a), 795(c), 793(d), 793(e).
ν_2	577, 582	550(b), 543(d), 542(e).
T	115,117	115(a), 117(b), 118(c), 117(d).

The experimental peak frequency values in Table 6 and Table 7 are in good agreement with those observed in reference[32,33].

Raman representations corresponding to the monoclinic structure of Ba_2WO_5 may be written as follows[29]

$$\Gamma(P2_1/n) = 6T(3A_g + 3B_g) + 6L(3A_g + 3B_g) + 2\nu_1(A_g + B_g) + 4\nu_2(2A_g + 2B_g) + 6\nu_5(3A_g + 3Bg \quad \ldots (4)$$

The Raman spectroscopy data also supports our X ray diffraction studies. The room-temperature comparative Raman spectra of LA-BMW for x = 0.10, 0.25, 0.50, 0.75 and 0.90 as shown in Fig. 4 also confirms that with increasing the value of x rhombohedral phase gradually increases and cubic phase gradually decreases. The signature cubic structural peaks at around 150 cm^{-1}, 450 cm^{-1} and 920 cm^{-1} progressively decreases with x concentration and finally minimises for the rhombohedral phase.

4 Conclusion

In the present work the effect of doping concentration 'x' on the structural and vibrational properties of complex double perovskite oxides $xLaAlO_3$–$(1-x)Ba(Mg_{1/2}W_{1/2})O_3$, synthesized by solid state reaction techniques are explored. Rietveld refinement of the X-ray refraction patterns show rhombohedral $R\bar{3}C(161)$ phase for $LaAlO_3$ and cubic Fm3m (225) phases for $Ba(Mg_{1/2}W_{1/2})O_3$. The vibrational properties of the samples are studied by Raman spectroscopy taken by 488 nm wavelength. Group theoretical study is performed to assigned the different vibrational modes of the samples in accordance with structural symmetry. The observed shifts of some vibration in some vibrations in the $xLaAlO_3$–$(1-x)Ba(Mg_{1/2}W_{1/2})O_3$ upon changing the doping concentration are tentatively explained.

References

1 Sasikala C, Durairaj N, Baskaran I, Sathyaseelan B & Henini M, *J Alloys Compd*, 712 (2017) 870.
2 Rajmohan S, Manikandan A, Jeseentharani V, Antony S A & Pragasam J, *J Nanosci Nanotechnol*, 16 (2016)1650.
3 Josephine B A, Manikandan A, Teresita V A & Antony S A, *Korean J Chem Eng*, 33 (2016) 1590.
4 Ahmed M A, Seoudi R & EI-Dek S I, *J Mol Struct*, 754 (2005) 41.
5 Zhandun V S & Zinenko V I, *Phys Solid State*, 57 (2015) 983.
6 VaslaS & Karppinen M, *Solid State Chem*, 43 (2015) 1.
7 Bull C L, Gleeson D & Knight K S, *J Phys Cond Matter*, 15 (2003) 4927.
8 Bettaibi A, Mnassri R, Selmi A, Rahmouni H, Chniba-Boudjada N, Cheikhrouhou A & Khirouni K, *J Alloy Compd*, 650 (2015) 268.
9 Mnassri R, Khelifi M, Rahmouni H, Selmi H A, Khirouni K & Chniba-Boudjada N, *Ceram Int*, 42 (2016) 6145.
10 Selmi A, Mnassri R, Cheikhrouhou-Koubaa W, Chniba-Boudjada N & Cheikhrouhou A, *Ceram Int,* 41(2015) 11221.

11 Rahmouni H, Cherif B, Baazaoui M & Khirouni K, *J Alloy Compd*, 575 (2013) 5.

12 Baron-Gonzalez A J, Frontera C, Garcia-Munoz J L, Rivas-Murias B & Blasco J, *J Phys Cond Matter*, 23 (2011) 496003.

13 Kato H, Okuda T, Okimoto Y & Tomioka Y, *Appl Phys Lett*, 81 (2002) 328.

14 Philipp J B, Majewski P, Alff L, Erb A, Gross R, Graf T, Brandt M S, Simon J, Walther T, Mader W, Topwal D & Sarma D D, *Phys Rev B*, 68 (2003) 144431.

15 Uratani Y, Shishidou T, Ishii F & Oguchi T, *Physica B*, 383 (2006) 9.

16 Lin Y Q& Chen X M, *J Am Ceram Soc*, 94 (2011) 782.

17 Lezaic M & Paldin S N A, *Phys Rev B*, 83 (2010) 024410.

18 Vulchev V, Vassilev L, Harizanova S, M Khristov, Zhecheva E & Stoyanova R, *J Phys ChemC,* 116 (2012) 13507.

19 Balakireva V B,Gorelov V P, Dunyushkina L A & Kuzmin A V, *Phys Solid State*, 61 (2019) 515.

20 Takahashi H, Ayusawa K & Sakamoto N, *J pn J Appl Phys*, 36 (1997) 5597.

21 Forst C J, Schwarz K & Blochl P E, *PhysRev Lett*, 95 (2005) 137602.

22 Winiarski M J, Kozie K, Sadecka K&Deren P J, *Solid State Commun*, 314 (2020) 113936.

23 Vu Q, Bondzior B, Stefanska D & Miniajluk N, *Materials*, 13 (2020) 1614.

24 Khalyavin D D, Salak A N, Senos A M, Mantas P Q & Ferreira V M, *J Am Ceram Soc*, 89 (2006) 1721.

25 Chen Y C,Wang Y N & Syu R Y, *J Mater Sci*, 27 (2016) 4259.

26 Oliveira M C, Gracia L, Nogueira I C, Gurgel M F C, Mercury J M R, Longo E & Andrés J, *Ceram Int*, 42 (2016) 10913.

27 Souza T G F, Ciminelli V S T & Mohallem N D S, *J Phys Conf Ser*, 733 (2016) 012039.

28 Ghosh B, Halder S & Sinha T P, *J Am Ceram Soc*, 97 (2014) 2564.

29 Rousseau D L, Bauman R P & Porto S P, *J Raman Spectra*, 10 (1981) 253.

30 Liegeois-Duyckaerts M & Tarte P, *Spectrochim Acta A*, 30 (1974) 1771.

31 Jayaraman A, Batlogg B & Van U L G B, *Phys Rev B*, 28 (1983) 4774.

32 Manjon F J, Errandonea1 D, Garro N & Kim J, *Phys Rev B*, 74 (2006) 144111.

33 Chance W M, Smith M D & Loye H C, *J Chem Cryst*, 45 (2014) 20.